

Precise tracking spectroscopy of beta-gamma cascade in nuclear decay

PandaX Collaboration: Zhe Yuan²⁶, Zihao Bo², Wei Chen², Xun Chen^{1,6,14}, Yunhua Chen^{13,14}, Chen Cheng⁷, Xiangyi Cui¹, Manna Deng²¹, Yingjie Fan²⁵, Deqing Fang²⁶, Xuanye Fu², Zhixing Gao², Yujie Ge²¹, Lisheng Geng^{7,8,9,10}, Karl Giboni^{2,14}, Xunan Guo⁷, Xuyuan Guo^{13,14}, Zichao Guo⁷, Chencheng Han¹, Ke Han^{2,6,14*}, Changda He², Jinrong He¹³, Houqi Huang⁵, Junting Huang^{2,14}, Yule Huang², Ruquan Hou^{6,14}, Xiangdong Ji¹⁹, Yonglin Ju^{4,14}, Xiaorun Lan¹², Chenxiang Li², Jiafu Li²⁰, Mingchuan Li^{13,14}, Peiyuan Li², Shuaijie Li^{2,13,14}, Tao Li⁵, Yangdong Li², Zhiyuan Li²¹, Qing Lin^{11,12}, Jianglai Liu^{1,3,6,14}, Yuanchun Liu², Congcong Lu⁴, Xiaoying Lu^{17,18}, Lingyin Luo¹⁵, Yunyang Luo¹², Yugang Ma²⁶, Yajun Mao¹⁵, Yue Meng^{2,6,14}, Binyu Pang^{17,18}, Ningchun Qi^{13,14}, Zhicheng Qian², Xiangxiang Ren^{17,18}, Dong Shan²⁴, Xiaofeng Shang², Xiyuan Shao²⁴, Guofang Shen⁷, Manbin Shen^{13,14}, Wenliang Sun^{13,14}, Xuyan Sun², Yi Tao²³, Yueqiang Tian⁷, Yuxin Tian², Anqing Wang^{17,18}, Guanbo Wang², Hao Wang², Haoyu Wang², Jiamin Wang¹, Lei Wang²⁷, Meng Wang^{17,18}, QiuHong Wang²⁶, Shaobo Wang^{2,5,14}, Shibo Wang⁴, Siguang Wang¹⁵, Wei Wang^{20,21}, Xu Wang¹, Zhou Wang^{1,6,14}, Yuehuan Wei²¹, Weihao Wu^{2,14}, Yuan Wu², Mengjiao Xiao², Xiang Xiao²⁰, Kaizhi Xiong^{13,14}, Jianqin Xu², Yifan Xu⁴, Shunyu Yao⁵, Binbin Yan¹, Xiyu Yan²², Yong Yang^{2,14}, Peihua Ye², Chunxu Yu²⁴, Ying Yuan², Youhui Yun², Xinning Zeng², Minzhen Zhang¹, Peng Zhang^{13,14}, Shibo Zhang¹, Siyuan Zhang²⁰, Shu Zhang²⁰, Tao Zhang^{1,6,14}, Wei Zhang¹, Yang Zhang^{17,18}, Yingxin Zhang^{17,18}, Yuanyuan Zhang¹, Li Zhao^{1,6,14}, Kangkang Zhao¹, Jifang Zhou^{13,14}, Jiaxu Zhou⁵, Jiayi Zhou¹, Ning Zhou^{1,6,14}, Xiaopeng Zhou⁷, Zhizhen Zhou², Chenhui Zhu¹²,

Marlom Ramalho^{28,29}, Jouni Suhonen^{28,30}

¹State Key Laboratory of Dark Matter Physics, Key Laboratory for Particle Astrophysics and Cosmology (MoE), Shanghai Key Laboratory for Particle Physics and Cosmology, Tsung-Dao Lee Institute & School of Physics and Astronomy, Shanghai Jiao Tong University, Shanghai 201210, China.

²State Key Laboratory of Dark Matter Physics, Key Laboratory for Particle Astrophysics and Cosmology (MoE), Shanghai Key Laboratory for Particle Physics and Cosmology, School of Physics and Astronomy, Shanghai Jiao Tong University, Shanghai 200240, China.

³New Cornerstone Science Laboratory, Tsung-Dao Lee Institute, Shanghai Jiao Tong University, Shanghai 201210, China.

⁴School of Mechanical Engineering, Shanghai Jiao Tong University, Shanghai 200240, China.

⁵SJTU Paris Elite Institute of Technology, Shanghai Jiao Tong University, Shanghai 200240, China.

⁶Shanghai Jiao Tong University Sichuan Research Institute, Chengdu 610213, China.

⁷School of Physics, Beihang University, Beijing 102206, China.

⁸Peng Huanwu Collaborative Center for Research and Education, Beihang University, Beijing 100191, China.

⁹International Research Center for Nuclei and Particles in the Cosmos & Beijing Key Laboratory of Advanced Nuclear Materials and Physics, Beihang University, Beijing 100191, China.

¹⁰Southern Center for Nuclear-Science Theory (SCNT), Institute of Modern Physics, Chinese Academy of Sciences, Huizhou 516000, China.

¹¹State Key Laboratory of Particle Detection and Electronics, University of Science and Technology of China, Hefei 230026, China.

¹²Department of Modern Physics, University of Science and Technology of China, Hefei 230026, China.

¹³Yalong River Hydropower Development Company, Ltd., 288 Shuanglin Road, Chengdu 610051, China.

¹⁴Jinping Deep Underground Frontier Science and Dark Matter Key Laboratory of Sichuan Province, Liangshan 615000, China.

¹⁵School of Physics, Peking University, Beijing 100871, China.

¹⁶Center for High Energy Physics, Peking University, Beijing 100871, China.

¹⁷Research Center for Particle Science and Technology, Institute of Frontier and Interdisciplinary Science, Shandong University, Qingdao 266237, China.

¹⁸Key Laboratory of Particle Physics and Particle Irradiation of Ministry of Education, Shandong University, Qingdao 266237, China.

¹⁹Department of Physics, University of Maryland, College Park, Maryland 20742, USA.

²⁰School of Physics, Sun Yat-Sen University, Guangzhou 510275, China.

²¹Sino-French Institute of Nuclear Engineering and Technology, Sun Yat-Sen University, Zhuhai 519082, China.

²²School of Physics and Astronomy, Sun Yat-Sen University, Zhuhai 519082, China.

²³School of Science, Sun Yat-Sen University, Shenzhen 518107, China.

²⁴School of Physics, Nankai University, Tianjin 300071, China.

²⁵Department of Physics, Yantai University, Yantai 264005, China.

²⁶Key Laboratory of Nuclear Physics and Ion-beam Application (MOE), Institute of Modern Physics, Fudan University, Shanghai 200433, China.

²⁷College of Nuclear Technology and Automation Engineering, Chengdu University of Technology, Chengdu 610059, China.

²⁸Department of Physics, University of Jyväskylä, P.O. Box 35, FI-40014 Jyväskylä, Finland.

²⁹School of Physics, Engineering and Technology, University of York, Heslington, York YO10 5DD, United Kingdom.

³⁰International Centre for Advanced Training and Research in Physics (CIFRA), P.O. Box MG12, 077125 Bucharest-Măgurele, Romania.

*Corresponding author(s). E-mail(s): ke.han@sjtu.edu.cn;

Abstract

Nuclear β decay, a sensitive probe of nuclear structure and weak interactions, has become a precision test bed for physics beyond the Standard Model (BSM), driven by recent advances in spectroscopic techniques. Here we introduce tracking spectroscopy of β - γ cascades, a method that reconstructs decay vertices while simultaneously detecting β particles and all associated de-excitation energies. Using the PandaX-4T detector operated as a tracking spectrometer, we obtain a precise and unbiased decay scheme of ^{214}Pb , a key background isotope in searches for dark matter and Majorana neutrinos. For the first time, transitions of ^{214}Pb to both the ground and excited states of ^{214}Bi are measured concurrently, revealing discrepancies in branching ratios of up to 4.7σ relative to previous

evaluations. Combined with state-of-the-art theoretical spectral shape calculations, these results establish a new benchmark for background modeling in rare-event searches and highlight the potential of tracking spectroscopy as a versatile tool for fundamental physics and nuclear applications.

1 Introduction

Understanding of nuclear β decay evolves with our knowledge of atomic, nuclear, and particle physics. From Rutherford's discovery of β -rays, to Fermi's β decay theory, to parity non-conservation, to the prosperous neutrino physics research, β decay is at the centre stage of fundamental physics research. More recently, β decay is used to constrain the neutrino wavepackets [1], test the CKM matrix unitarity [2], probe new electro-weak coupling [3], and measure the neutrino mass [4].

At the forefront of *beta*-decay research is spectroscopy, which includes the measurement of the β spectrum (β spectroscopy) and the relative intensities of de-excitation γ rays (γ spectroscopy). β -spectroscopy includes a wealth of traditional and new experimental techniques, such as ion traps [5], cryogenic calorimeters [6], electrostatic filters [4], and cyclotron resonance spectroscopy [7]. The γ -spectroscopy is widely used to determine nuclear structure and to identify trace isotopes in materials. Total-absorption gamma spectroscopy (TAGS), measuring γ rays' total energy with high efficiency and thus avoiding the Pandemonium Effect [8], has a direct impact on reactor antineutrino flux estimation and nuclear astrophysics [9]. However, no mature methods exist for a simultaneous β and γ spectroscopy.

We propose a novel spectroscopic measurement of β particles and their subsequent de-excitation energies, demonstrated by a liquid xenon time projection chamber (TPC) in the PandaX-4T experiment. With a radioactive sample doped in the xenon volume, energies from all the decay products (excluding neutrinos), including β , de-excitation γ s, and internal conversion electrons (ICEs), are measured by the xenon TPC. The xenon detector can also measure the local energy deposition vertices with millimetre precision. Compared with scintillator-based TAGS, the tracking spectrometer enables the accurate and unbiased determination of the decay scheme through simultaneous β - γ -ICE measurements, improved detection efficiency, and better energy resolution. Combined with theoretical spectral shape calculations, the tracking spectrometer yields the β spectra of all major decay modes using a single detector and dataset.

The prowess of tracking spectroscopy is demonstrated by the precise measurement of ^{214}Pb β decay, which is one of the most challenging backgrounds for dark matter detection and neutrino physics in the liquid xenon detectors, such as PandaX-4T [10]. ^{214}Pb is a decay product of radon-222 (^{222}Rn), which emanates from the inner surfaces of the detector and its surrounding components. In liquid xenon TPCs, decades of extensive purification efforts have achieved an extraordinary reduction in radon concentrations, reaching levels as low as 0.1 ^{222}Rn atoms per mole of xenon. Yet, ^{214}Pb β particles continue to dominate the background in next-generation detectors. During a dedicated ^{222}Rn calibration campaign, PandaX-4T acquired approximately half a million ^{214}Pb decay events from May 27 to June 9, 2022. With a state-of-the-art β spectrum calculation, we fit the data iteratively to reach a best fit of decay branching ratios (BRs) and spectral shapes. The result represents the most precise measurement of the ^{214}Pb β decay scheme, a first demonstration of tracking spectroscopy to improve the precision of nuclear data.

2 The challenge of β decay spectroscopy

β decay (here we specifically refer to β^- decay) is a weak interaction process in which a neutron in a nucleus decays to a proton and emits an electron (called a β particle) and an antineutrino. The daughter nucleus may be in the ground state (GS) and various excited states (ESs). The subsequent de-excitation releases energy via (cascades of) γ -rays or ICEs. For example, Fig. 1a lists the major ^{214}Pb decay branches to the GS and ESs of ^{214}Bi with a Q-value of 1019 keV. We denote the branches based on excitation energy as GS, ES₂₉₅, ES₃₅₂, ES₅₃₄, and ES₈₃₉, respectively. Emitted β spectra from different branches overlay with each other with the same starting energy of 0 keV, which makes β -spectroscopy nearly impossible to decompose each component, as shown in Fig. 1b. ICEs further pollute the β spectra. The relative intensity measured by γ -spectroscopy, as illustrated in Fig. 1c, does not directly reflect the decay BRs. Theoretical calculation of the internal conversion coefficient, the ratio of ICEs to γ rays emitted during the de-excitation of each excited state, and consideration of cascade de-excitation via intermediate ESs are required to calculate the BRs.

Spectroscopic detection of β and γ introduces additional uncertainties in the decay scheme. The energy loss of β particles in the trajectory from the radioactive source to the detector, along with energy-dependent detector efficiency and linearity, inadvertently distorts the β spectra. Similar challenges arise in the measurement of γ intensity.

Fig. 1a lists evaluated BRs from Nuclear Data Sheets (NDS) published in 2021 [11] and 2009 [12], as well as BRs from the DDEP database, the de facto standard in metrology [13]. BRs of the ESs are assessed based on γ intensity and internal conversion coefficient [14]. The GS ratio is calculated from the ES values, requiring that the total probability be unity [15]. The uncertainties of BRs in NDS2021 originate from the evaluation process [14], while no uncertainties are quoted in the other two databases. Significant differences in the central values of BRs across different nuclear databases highlight the challenges in β decay spectroscopy.

Theoretical calculation of β spectra is highly non-trivial, especially for the forbidden decays, such as GS, ES_{295} , ES_{534} of ^{214}Pb . The β energy spectrum shape is determined by experimental inputs including β end-point energy and BRs, and theoretical treatment of the nuclear structure of the initial and final states, the quenching effect of the axial vector coupling constant g_A , the atomic exchange effect, etc. Those effects are treated differently in various theoretical calculations and cause noticeable spectral shape differences [10]. A rigorous, consistent treatment of all branches based on reliable experimental inputs is urgently needed.

The spectral shapes of different branches and their corresponding BRs in ^{214}Pb decay directly influence the physics sensitivities of xenon detectors. For Weakly Interacting Massive Particles (WIMPs) and solar proton-proton fusion neutrino searches, the most effective energy windows are below 30 keV and 200 keV, respectively, where the ^{214}Pb GS decay spectrum is one of the most dominating backgrounds. The β decay spectrum at the MeV end, depending on the individual spectrum of each ES decay as well as the branching ratios, has become one of the leading systematic uncertainties for measuring double β decay half-lives of Xe isotopes [16, 17], as well as searches for BSM physics [18].

3 PandaX-4T TPC as a tracking spectrometer

The PandaX-4T detector is a cylindrical, liquid xenon TPC with an active volume (AV) of 118.5 cm in diameter and 118.5 cm in height, which is encompassed by an electric field cage on the side. A total of 3.7 tonnes of natural xenon is enclosed in the AV. Two photomultiplier (PMT) arrays are installed at the top and bottom of the AV for signal readout. A detailed account of the detector can be found in Ref. [19].

The TPC can measure an event's three-dimensional position and energy. An energy deposition causes prompt scintillation light signals ($S1$) and ionization electrons, which are converted to a delayed electroluminescence signal ($S2$) at the top of the AV. Both $S1$ and $S2$ are recorded by the PMT arrays. The event's position in the horizontal XY plane can be reconstructed from the relative numbers of photons detected by each PMT in the top

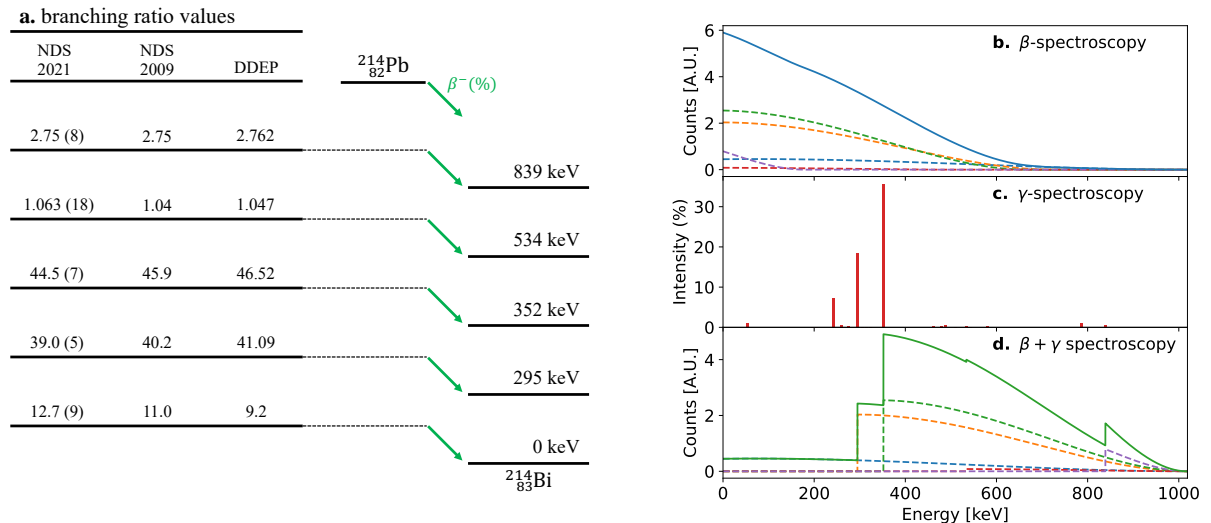


Fig. 1 a. The β decay scheme of ^{214}Pb and the corresponding branching ratios in different databases. Uncertainties follow the NDS2021 values in parentheses. No uncertainties are quoted in the other two databases. b.c.d. Illustration of β decay spectroscopic techniques. The spectra do not include detector effects.

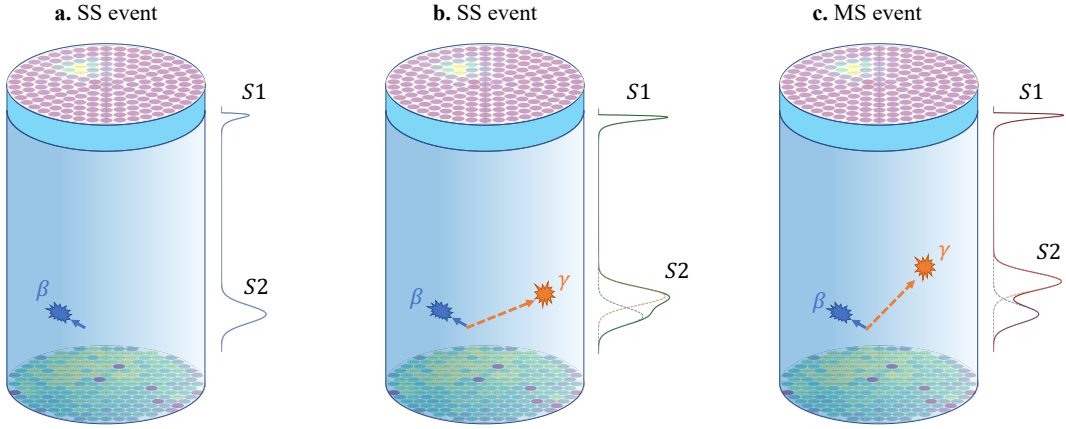


Fig. 2 Schematic diagrams of signal types of GS and ES decays. a. GS decays with one single S2 are identified as SS events. b. ES decays with overlapping S2s are identified as SS events. c. ES decays with separated S2s are identified as MS events.

array. The vertical (Z direction) position is determined from the time delay between $S1$ and $S2$ signals. The total energy of an event is computed by combining the charges of $S1$ and $S2$. The detector's energy response is calibrated by external radioactive γ sources including ^{137}Cs , ^{60}Co , and ^{232}Th . Systematic variations in energy reconstruction with position are monitored and corrected using the internal calibration source $^{83\text{m}}\text{Kr}$.

PandaX-4T TPC functions as a tracking spectrometer for ^{214}Pb decay BR measurements. For ES decay of ^{214}Pb in the active volume, the xenon detector measures both the β and γ particles. The majority of emitted γ -rays deposit the full energy within the AV since the most energetic 839 keV γ -rays have an attenuation length of 6 cm in liquid xenon, approximately 1/20 of the TPC diameter. The measured energy spectrum of an ES decay starts from the full energy of the de-excitation γ -rays, as shown in Fig. 1d. For example, the ES_{295} β spectrum is shifted up by 295 keV. The shifted spectra of ES decays overlay the GS spectrum, with relative intensities determined by the corresponding BRs. The effective attenuation of xenon also prevents external γ -rays from entering the central cleanest fiducial volume (FV).

The $\beta + \gamma$ /ICEs events measured with PandaX-4T are grouped to single-site (SS) and multiple-site (MS) events by counting the number of identifiable peaks in the $S2$ waveforms. Fig. 2 demonstrates the SS and MS nature of different scenarios. The β particle from ^{214}Pb effectively appears as a single energy deposition in xenon. The corresponding $S2$ waveform has one single peak, as shown in Fig. 2a. For ^{214}Pb ES decays, the emitted γ -ray may scatter multiple times. Depending on the vertical positions of the β and γ vertices, the β - γ cascade may appear as an SS or MS event (Fig. 2). The discrimination of SS and MS events further helps PandaX-4T TPC to identify the energy deposits from different decay branches of ^{214}Pb .

4 ^{214}Pb data and fitted branching ratios

High-quality ^{214}Pb β decay data were acquired in a dedicated ^{222}Rn injection campaign. During the campaign, the average activity of ^{214}Pb was approximately 0.5 Bq in the FV. In total, we have accumulated half a million ^{214}Pb decay events with a signal-to-background ratio of more than 10 after all data selection procedures.

The data production and event selection follow procedures similar to those in PandaX-4T's previous publications [16, 17]. We utilize the SS spectrum from 20 keV to 1 MeV (Fig. 3a) and MS spectrum from 260 keV to 1 MeV (Fig. 3b), with events selected from the central cleanest 1118 ± 24 kg xenon. Two dominating mono-energetic peaks at 164 keV (from $^{131\text{m}}\text{Xe}$) and 236 keV (from $^{129\text{m}}\text{Xe}$ and ^{127}Xe) in the SS spectrum are due to preceding neutron calibrations. Details of the data quality cuts and SS identification criteria are provided in the Methods section. The SS identification criteria applied to both Monte Carlo (MC) simulation and external γ calibration data select statistically identical fractions of SS events, validating the SS criteria. The differences in SS (MS) fractions between MC and γ data in the ROI are averaged to be 3.42% (3.31%), which are conservatively adopted as systematics for all signal and background components.

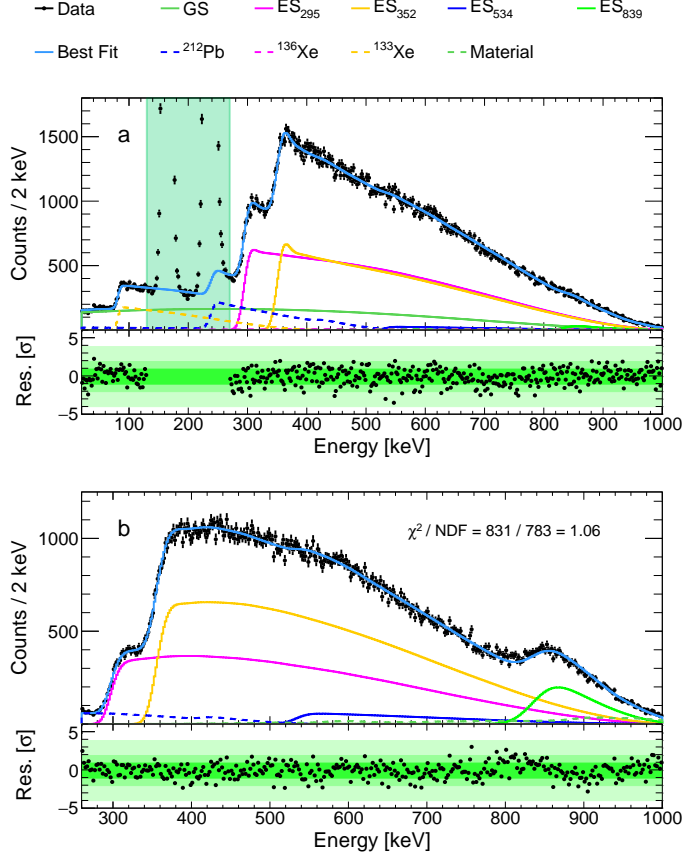


Fig. 3 The ^{214}Pb data and the final best-fit are shown for SS (a) and MS (b), with a bin size of 2 keV. The horizontal axis represents the reconstructed energy in the data. The shaded green area in (a) represents the excluded region. The lower panel in each figure shows the fit residuals together with $\pm 1\sigma$, $\pm 2\sigma$, and $\pm 4\sigma$ bands.

The five major ^{214}Pb β spectral curves are calculated theoretically and convoluted with the detector response of PandaX-4T. The β spectral shapes of each β transition were computed using the state-of-the-art β decay code [20] with updated atomic exchange corrections and refinements of the next-to-leading-order β formalism presented in Ref. [21, 22]. Out of the five decays of interest, only the ES_{839} transition is an allowed decay and has a universal spectral shape [23]. The shapes of all other branches depend on the experimental BRs and modelling parameters [24–26]. An initial set of theoretical β curves are calculated based on the BRs from NDS2021. Theoretical curves are then used to generate simulated SS and MS curves after going through the Monte Carlo simulation pipeline, which incorporates energy deposition and TPC detector response. More details of the theoretical calculation and the simulated curves can be found in Methods.

We performed a simultaneous binned likelihood fit of SS and MS data spectra with simulated curves to extract BRs of the five ^{214}Pb decay branches. The SS spectrum ranges from 20 to 1000 keV, with 130 to 270 keV excluded. The MS spectrum starts from 260 keV. Nuisance parameters, such as efficiency and energy response, are constrained with Gaussian penalty terms in the likelihood function.

The output BRs from the fit are used as input to calculate new sets of theoretical curves, which are then refitted to the data. The iterative fit processes are repeated three times, and the fitted BRs are stable. The final fit is shown in Fig. 3, with reduced $\chi^2 = 1.06$. The final BR values for the five decay branches are $11.3\% \pm 0.5\%$ (GS), $39.5\% \pm 1.2\%$ (ES_{295}), $45.0\% \pm 1.2\%$ (ES_{352}), $1.9\% \pm 0.2\%$ (ES_{534}), and $2.4\% \pm 0.1\%$ (ES_{839}). The uncertainty of the GS BR is about half of the previously reported value. What is more critical for the low-energy background budget in the WIMP ROI, the central value is as much as 11% smaller than the one in the NDS2021 database. The BR to the ES_{534} (ES_{839}) is 79% (13%) different from the NDS2021 values, representing a 4.7σ (2.4σ) deviation.

The fit results are cross-validated with alternative fit strategies. We have performed a fit with the SS spectrum only, and the results are consistent with the values shown above. Background contributes insignificantly to the spectra in Fig. 3. The total counts of material γ s, ^{136}Xe , ^{133}Xe , and ^{212}Pb are about $(7.0 \pm 1.4)\%$ of the ^{214}Pb events.

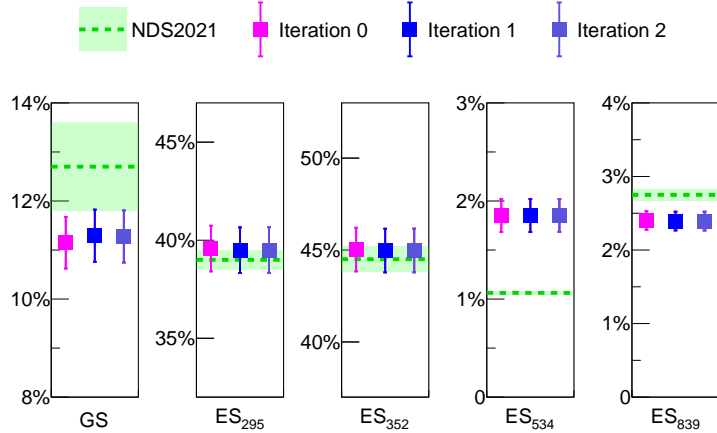


Fig. 4 The fitted branching ratio of ^{214}Pb β decay of each iterations. The solid square is the fitted result with error bars (1σ). The NDS2021 values are shown as the green dashed line with the uncertainty bands.

No significant differences are observed if we fix the background contribution from detector materials, the energy resolution, or the energy offset to the input value.

5 Summary and outlook

We have introduced the tracking spectroscopy, a spectroscopic technique to simultaneously detect the energy release of the β , γ s, and ICEs, a feat previously unattainable by traditional β decay measurements. With the vertex reconstruction capability, a tracking spectrometer can measure the local energy deposition. Tracking spectrometers directly measure the decay to GS and ESs. The consistent treatment of GS and ESs with one set of measurement data circumvents detector normalization ambiguity. For the ESs, tracking spectrometers measure both the γ s and ICEs with nearly 100% efficiency, evading the challenges of modelling the decay scheme and correcting the γ detection efficiency.

We have precisely measured the branching ratios of ^{214}Pb β decay using the PandaX-4T TPC detector. With a dedicated calibration campaign, we have accumulated nearly half a million ^{214}Pb events in the ROI, with the number of background events fewer than one-tenth that of the ^{214}Pb events. The measurement uncertainty is well controlled thanks to the high-quality data and rigorous detector response studies of the PandaX-4T detector. Our measured BRs differ significantly from widely used database values. Most noticeably, the branching ratio to the ES_{534} is 79% times higher than the NDS2021 value, and the difference accounts for a 4.7σ deviation. The notable 11% difference of the BR to GS between NDS2021 and our result is also critical since the difference is preserved when extrapolating the ^{214}Pb contribution in the WIMP ROI from the high energy spectrum.

We also calculate a new set of β spectra for the five major branches by combining our measured BRs and the latest state-of-the-art nuclear shell model. The parameters in the spectrum calculations, tuned to match the measured BRs, agree with previous publications, further validating our measurement [24, 27]. The new spectra will serve as the benchmark for ^{214}Pb background modelling in xenon detectors, improving the sensitivities of ultra-rare event searches in dark matter and neutrino experiments.

Our study represents an initial step toward demonstrating the full potential of the xenon TPC as a tracking spectrometer. More general isotopes could be introduced into liquid xenon either as particulates or through novel doping techniques. With advanced reconstruction algorithms, the individual β and γ energies of multi-site events could be resolved, thereby reducing systematic uncertainties in the measurements.

More generally, tracking spectrometer may provide more insight in nuclear structure and serve as a direct probe of physics beyond the Standard Model with high-precision β -decay measurement. A liquid-xenon TPC could serve as a versatile tracking spectrometer for cascades of γ , neutron, and charged particles in nuclear decays. A dedicated setup—with a smaller active mass and improved energy and position resolution—enables a broad range of applications in fundamental and applied nuclear science.

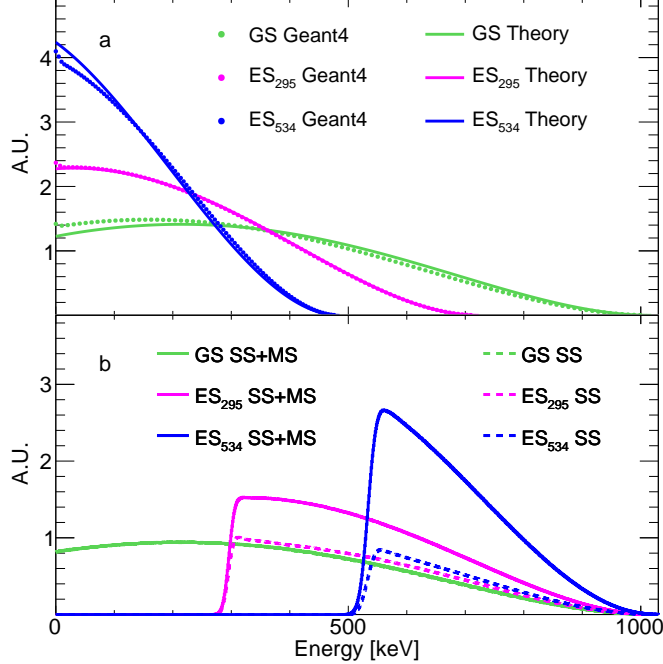


Fig. 5 Comparison of the energy response spectra of the detector due to the decay branches of GS, ES₂₉₅, and ES₅₃₄ using Geant4 default β energy spectra and using theoretical β energy spectra. The top graph is the β energy spectra, and the bottom is the detector response energy spectra.

6 Methods

6.1 Signal model of the β spectra

The nuclear wave functions of the initial 0^+ ground state of ^{214}Pb and the daughter's ground and excited states in the final nucleus ^{214}Bi were calculated using the nuclear shell model (NSM), using the code KSHELL [28] with the *khpe* NSM Hamiltonian [29] found in the code NuShellX@MSU [30]. There, the model space consists of $1h_{9/2}$, $2f_{7/2}$, $2f_{5/2}$, $3p_{3/2}$, $3p_{1/2}$ and $1i_{13/2}$, for protons, and $1i_{11/2}$, $2g_{9/2}$, $2g_{7/2}$, $3d_{5/2}$, $3d_{3/2}$, $4s_{1/2}$ and $1j_{15/2}$ for neutrons. No configuration truncations were made in the calculations. The β spectral shapes of each β transition were computed using the state-of-the-art β decay code [20] with updated atomic exchange corrections [22], developed for allowed decays and herein as a surrogate for the forbidden non-unique decays as well as the allowed branch and other refinements of the next-to-leading-order β formalism presented in [21]. The value of the vector-type so-called small relativistic nuclear matrix element (sNME) [31], was fitted for each β transition to reproduce the corresponding partial half-life. This procedure accounts for contributions from orbitals outside the defined model space (the frozen core and orbitals above the model space), a limitation of the NSM. This method yields two possible values for the sNME for each β transition, as discussed in [24–26]. These sNME can be smaller or larger than the so-called CVC (Conserved Vector Current) value of the sNME (see, e.g., [24, 31]). In the calculations presented here, one set of the sNME has lower values (lower set) than the CVC value, while the other set has higher values (upper set). These sNME are active in the decays to the 1^- GS and the 295 keV and 534 keV excited 1^- states. As for the transition to the excited 0^- state at 352 keV of excitation, there is no sNME since the decay couples a $J_i = 0$ to $J_f = 0$ state, thus no vector components are present. However, with $\Delta J = 0$ another contribution appears, the mesonic enhancement factor ε_{MEC} . This enhancement factor has been charted, e.g., in [32], and here its value was used (together with g_A) to fix the branching ratio of this transition. The transition to the 839 keV 1^+ state is an allowed one and has a universal spectral shape [23]. All the involved transitions feature the weak axial coupling g_A and transitions to the 1^- states the weak vector coupling g_V . For g_V we have used the CVC value $g_V = 1.0$. Given the persistent theoretical uncertainty in the effective value of g_A , we performed the computations for each transition across a range of values from 0.6 to 1.2 in 0.1 increments.

Fig. 5a shows the comparison of GS, ES₂₉₅ and ES₅₃₄ spectra of the latest theoretical calculation and the Geant4 model. Fig. 5b takes into account the de-excitation γ -ray(s), and the expected spectra are shifted by the

excitation energy in the PandaX-4T detector. The curves included energy resolution and SS/MS discrimination for both the theoretical calculation and Geant4. Since the mean free path of the 534 keV γ is relatively long, more events are tagged as MS than SS.

The theoretical curves are grouped as lower and upper sets. The lower set has GS and ES_{295} spectra generated with smaller sNME values, the ES_{534} spectrum with a larger sNME value, whilst the upper set has all three spectra with larger sNME values. Although the spectra were computed for g_A values from 0.6 to 1.2, a value of $g_A = 1.0$ was adopted for this work. This choice is informed by the extensive study of first-forbidden β decay transitions in the lead region by Warburton [27], which suggests a quenched value of $g_A \approx 1.0$. For transitions where $\Delta J = 0$, both g_A and the mesonic enhancement factor, ε_{MEC} , contribute. With g_A fixed at 1.0, ε_{MEC} was adjusted to reproduce the experimental branching ratios. This procedure resulted ε_{MEC} values of 2.117 and 2.153 for the lower and upper sets, respectively, for the last iteration, consistent with Warburton's [27] value 2.01. These results are also consistent with our previous findings where the value $\varepsilon_{\text{MEC}} \approx 2.2$ for $g_A = 1.0$ was recorded in [24]. The values are slightly reduced from those found in the earlier work because the present calculations now incorporate more spectral corrections, such as improved atomic exchange corrections relevant for low electron energies.

6.2 ^{214}Pb data

The ^{214}Pb data production and event selection follow similar procedures to those in PandaX-4T's previous publications [16, 17]. We utilize the SS spectrum from 20 keV to 1 MeV and the MS spectrum from 260 keV to 1 MeV for the data analysis. Position of each event is reconstructed based on the S2 charge patterns on the top PMT array. For an MS event, the charge of $S1$, denoted as Q_{S1} , is partitioned to Q_{S1i} according to the corresponding charge of each $S2_i$ ($i = 1, 2, \dots$, denotes the i -th deposition). Each Q_{S1i} is corrected for position dependence and then summed up to obtain Q_{S1}^c . The charge of each $S2_i$ on the bottom PMT array Q_{S2bi} is applied with a mapping and electron-drift-lifetime correction, and then calibrated according to the external γ sources to derive the summed charge Q_{S2b}^c . The energy of each measured event is calculated from the (Q_{S1}^c, Q_{S2b}^c) pair. The S2 charge on the top PMT array is not used in energy reconstruction due to PMT signal saturation at MeV range [16].

Pb decay events are selected in the central cleanest FV, which is defined as $R^2 \in [0, 2000 \text{ cm}^2]$ and $Z \in [-307 \text{ mm}, 307 \text{ mm}]$. The zero point is defined as the geometric center of the xenon volume. The mass of liquid xenon in the FV is $1118 \pm 24 \text{ kg}$, calculated by the percentage of uniformly distributed $^{83\text{m}}\text{Kr}$ in the FV with respect to the full AV [17]. Overlapping events, defined as events with another $S1$ signal in the time window of 1 ms before the event to the end of the event, are removed from the spectrum. β -particles from ^{214}Bi (^{212}Bi), daughter of ^{214}Pb (^{212}Pb), are removed from the spectrum by the coincidence with the α -particles of the subsequent ^{214}Po (^{212}Po), which has a half-life of 164.3 (0.3) μs . With a coincidence window of 2.5 ms window ahead of the $S1$ time of an α event, we eliminate 99.9975% (100%) of the ^{214}Bi (^{212}Bi) β events.

The data quality cuts and SS identification criteria are the same as Ref. [17]. The efficiency of data quality cuts, which eliminate noise and select electron recoil events, is $99.87 \pm 0.03\%$ for SS and $99.86 \pm 0.03\%$ for MS. The SS and MS discrimination is modelled with BambooMC, a Geant4-based simulation package developed by PandaX [33]. The SS and MS fractions for both signal and background events within the region of interest (ROI) are calculated. Energy depositions simulated in Geant4 are converted into individual S2s, which are then smeared in time with drift-time-correlated Gaussian diffusion measured in the data. The pseudo-S2 waveforms are then piped through the SS/MS discrimination algorithm. The resulting SS and MS spectra are compared to the corresponding spectra in the calibration runs. No systematic deviation is observed as a function of energy, and the average difference in the SS (MS) fraction is 3.42% (3.31%), which is conservatively adopted as systematics for all signal and background components.

In our ROI, the background contribution originates from radioactive contamination of the detector components and of the liquid xenon. γ -rays emitted from ^{60}Co , ^{40}K , ^{232}Th , and ^{238}U in the detector components may reach the FV, but the intensity is significantly reduced due to xenon attenuation. The contributions are grouped with the same input and constraints as documented in Ref. [16]. ^{136}Xe is one of the isotopes of xenon and undergoes double β decay. The contributions and constraints from ^{136}Xe are determined using the half-life measurements in PandaX-4T [16]. During the ^{222}Rn injection process, a trace amount of ^{220}Rn is mixed with the xenon as well. In the detector, ^{133}Xe is introduced by activation during neutron calibrations. The activities of ^{212}Pb and ^{133}Xe are float in the fit. Two dominating mono-energetic peaks at 164 keV (from $^{131\text{m}}\text{Xe}$) and 236 keV (from $^{129\text{m}}\text{Xe}$ and ^{127}Xe) in the SS spectrum are due to preceding neutron calibrations. Both peaks are excluded in the fit.

Table 1 The total background contributions in the ROI (SS + MS). The fitted counts are obtained from the iteration 2 lower and iteration 2 upper β spectra fitting.

Components	Expected	Fitted (lower)	Fitted (upper)
Material	5206 ± 223	6008 ± 254	6002 ± 250
^{136}Xe	2392 ± 110	2556 ± 132	2799 ± 139
^{212}Pb	float	17777 ± 841	18503 ± 845
^{133}Xe	float	6110 ± 308	6600 ± 316
Overall efficiency (SS)	3.4%	$2.7\% \pm 3.1\%$	$8.3\% \pm 3.1\%$
Overall efficiency (MS)	3.3%	$5.7\% \pm 3.2\%$	$3.0\% \pm 3.0\%$

6.3 Fit and results

We performed a simultaneous fit with SS and MS spectra, allowing each of the five major ^{214}Pb decay branches to float freely. The SS spectrum ranges from 20 to 1000 keV, excluding 130 to 270 keV. The MS spectrum starts from 260 keV. We employ a binned likelihood fit method, with the likelihood function constructed as

$$L = \prod_{r=0}^1 \prod_{i=1}^{N_{\text{bins}}} \frac{(N_{r,i})^{N_{r,i}^{\text{obs}}} e^{-N_{r,i}}}{N_{r,i}^{\text{obs}}!} \mathcal{G}(\mathcal{M}_r; \mathcal{M}_0^0, \Sigma_r) \cdot \prod_{j=1}^{N_G} G(\eta_j; 0, \sigma_j), \quad (1)$$

where $N_{r,i}$ and $N_{r,i}^{\text{obs}}$ are the expected and observed events numbers of the i_{th} energy bin in the SS or MS spectrum ($r = 0$ or 1), respectively. The Gaussian penalty term $\mathcal{G}(\mathcal{M}; \mathcal{M}_0, \Sigma_r)$ of the energy response contains the five-parameter \mathcal{M}_0 and the covariant matrix Σ_r . The Gaussian penalty terms $G(\eta_j; 0, \sigma_j)$ constrain the nuisance parameters η_a and η_b , which are the relative uncertainties of the overall efficiency and the background components, respectively. $N_G = 14$ is the number of Gaussian-constrained nuisance parameters. For both the SS and MS spectra, the expected counts per bin N_i is defined as

$$N_i = (1 + \eta_a) \cdot [\sum_{s=1}^{N_{\text{sig}}} n_s \cdot S_{s,i} + \sum_{b=1}^{N_{\text{bkg}}} (1 + \eta_b) \cdot n_b \cdot B_{b,i}], \quad (2)$$

where n_s and n_b are the total counts of signal s and background component b , respectively. The corresponding $S_{s,i}$ and $B_{b,i}$ are the i_{th} bin values of the normalized energy spectrum.

The ^{214}Pb spectra are convoluted with the detector response of PandaX-4T. We iteratively fit the experimental spectra with theoretical curves. Two initial sets of theoretical β spectra, labeled as the ‘lower’ and ‘upper’ sets based on the most likely sets of sNME choices, are calculated based on the BRs from NDS2021. New sets of spectra are then regenerated with the BRs from fits and used in another iteration of fits until the fitted BRs converge. The iterations converged after three rounds. The initial fit is named Iteration 0, and subsequent iteration increases the number by 1. In the iteration fits, the lower set of spectra is favoured, with a fit $\Delta\chi^2 = 45$ between upper and lower sets in Iteration 0. The Iteration 2 fit results with a lower set of spectra are shown in Fig. 3, with reduced $\chi^2 = 1.06$. Finally, the values in Iteration 2 for the five major decay branches are $11.3\% \pm 0.5\%$ (GS), $39.5\% \pm 1.2\%$ (ES_{295}), $45.0\% \pm 1.2\%$ (ES_{352}), $1.9\% \pm 0.2\%$ (ES_{534}), and $2.4\% \pm 0.1\%$ (ES_{839}). The BR to ES_{534} (ES_{839}) is 4.7σ (2.4σ) away from the NDS2021 value. What is more critical for the low-energy background budget in the WIMP ROI, the BR to GS is as much as 11% smaller than the NDS2021 value.

The contributions of other background components, summarized in Table 1, are consistent with their expected values, except for material and overall efficiency (MS), which are slightly pulled upward by 2.3σ and 1.7σ .

The energy response is modelled with five parameters. The energy resolution is modelled as a Gaussian function with the width $\sigma(E)$ constructed as $\frac{\sigma(E)}{E} = \frac{a}{\sqrt{E}} + b \cdot E + c$, with energy in the unit of keV. The energy scale is defined as $E = d \cdot \hat{E} + e$ to account for possible bias with respect to the reconstructed energy \hat{E} . The measured energy spectrum is a convolution of the true energy spectrum with the five-parameter response model. The

Table 2 Summary of sources of systematic uncertainties. \mathcal{M}_0 represents the 5-parameter detector response model (see text), with means and uncertainties determined from calibration fit.

Sources		Values
\mathcal{M}_0 (SS)	a_0 [$\sqrt{\text{keV}}$]	0.48 ± 0.03
	b_0 [keV^{-1}]	$(6.1 \pm 1.0) \times 10^{-6}$
	c_0	$(-2.3 \pm 2.2) \times 10^{-3}$
\mathcal{M}_0 (MS)	d_0	0.9984 ± 0.0004
	e_0 [keV]	0.72 ± 0.56
	a_0 [$\sqrt{\text{keV}}$]	0.41 ± 0.18
\mathcal{M}_0 (MS)	b_0 [keV^{-1}]	$(14.0 \pm 2.1) \times 10^{-6}$
	c_0	$(-3.7 \pm 8.6) \times 10^{-3}$
	d_0	0.9995 ± 0.0005
Overall efficiency (SS)	e_0 [keV]	0.66 ± 0.87
	^{232}Th SS fraction	$(49.2 \pm 3.4)\%$
	Quality cut	$(99.87 \pm 0.03)\%$
Overall efficiency (MS)	^{232}Th MS fraction	$(57.8 \pm 3.3)\%$
	Quality cut	$(99.86 \pm 0.03)\%$
Background model		Table 1

parameters and their uncertainties are determined by fitting the peaks of 41.5 keV (from $^{83\text{m}}\text{Kr}$), 164 keV (from $^{131\text{m}}\text{Xe}$), 236 keV (from ^{127}Xe and $^{129\text{m}}\text{Xe}$) obtained during calibration runs, and the 1460 keV peak (from ^{40}K), 1764 keV peak (from ^{238}U chain), 2615 keV peak (from ^{232}Th chain) outside the ROI. These calibration peaks are completely uncorrelated with those used in the final spectral fit. The extracted values $\mathcal{M}_0 = (a_0, b_0, c_0, d_0, e_0)^T$ and uncertainties of the parameters are used as priors, together with the 5×5 covariance matrix Σ_r in fitting the ^{214}Pb spectra.

Acknowledgement

The PandaX project is supported in part by grants from National Key R&D Program of China (Nos. 2023YFA1606200, 2023YFA1606202), National Science Foundation of China (Nos. 12090060, 12090062, U23B2070), and by Office of Science and Technology, Shanghai Municipal Government (grant Nos. 21TQ1400218, 22JC1410100, 23JC1410200, ZJ2023-ZD-003). PandaX collaboration thanks for the support by the Fundamental Research Funds for the Central Universities. We also thank the sponsorship from the Chinese Academy of Sciences Center for Excellence in Particle Physics (CCEPP), Thomas and Linda Lau Family Foundation, New Cornerstone Science Foundation, Tencent Foundation in China, and Yangyang Development Fund. M. Ramalho acknowledges support by the Oskar Huttunen Foundation, grants of computer capacity from the Finnish Grid and Cloud Infrastructure (persistent identifier urn:nbn: fi:research-infras-2016072533), and the support by CSC-IT Center for Science, Finland, for generous computational resources. J. Suhonen acknowledges support from the NEPTUN project (PNRR-I8/C9-CF264, Contract No. 760100/23.05.2023 of the Romanian Ministry of Research, Innovation and Digitization). Finally, we thank the CJPL administration and the Yalong River Hydropower Development Company Ltd. for indispensable logistical support and other help.

References

[1] Smolsky, J., *et al.*: Direct experimental constraints on the spatial extent of a neutrino wavepacket. *Nature* **638**(8051), 640–644 (2025) <https://doi.org/10.1038/s41586-024-08479-6> arXiv:2404.03102 [nucl-ex]

[2] Towner, I.S., Hardy, J.C.: The evaluation of V_{ud} and its impact on the unitarity of the Cabibbo-Kobayashi-Maskawa quark-mixing matrix. *Rept. Prog. Phys.* **73**, 046301 (2010) <https://doi.org/10.1088/0034-4885/73/4/046301>

[3] Burkey, M.T., *et al.*: Improved Limit on Tensor Currents in the Weak Interaction from $\text{Li}^8\beta$ Decay. *Phys. Rev. Lett.* **128**(20), 202502 (2022) <https://doi.org/10.1103/PhysRevLett.128.202502> arXiv:2205.01865 [nucl-ex]

[4] Aker, M., *et al.*: Direct neutrino-mass measurement based on 259 days of KATRIN data. *Science* **388**(6743), 9592 (2025) <https://doi.org/10.1126/science.adq9592> arXiv:2406.13516 [nucl-ex]

[5] Alcalá, G.A., *et al.*: Study of the Beta Spectrum Shape of Rb^{92} and Cs^{142} Decays for the Prediction of Reactor Antineutrino Spectra. *Phys. Rev. Lett.* **135**(14), 142502 (2025) <https://doi.org/10.1103/PhysRevLett.135.142502> arXiv:2406.13516 [nucl-ex]

[6] Pagnanini, L., *et al.*: Simultaneous Measurement of the Half-Life and Spectral Shape of $\text{In}^{115}\beta$ Decay with an Indium Iodide Cryogenic Calorimeter. *Phys. Rev. Lett.* **133**(12), 122501 (2024) <https://doi.org/10.1103/PhysRevLett.133.122501> arXiv:2401.16059 [nucl-ex]

[7] Ashtari Esfahani, A., *et al.*: Tritium Beta Spectrum Measurement and Neutrino Mass Limit from Cyclotron Radiation Emission Spectroscopy. *Phys. Rev. Lett.* **131**(10), 102502 (2023) <https://doi.org/10.1103/PhysRevLett.131.102502> arXiv:2212.05048 [nucl-ex]

[8] Hardy, J.C., Carraz, L.C., Jonson, B., Hansen, P.G.: The essential decay of pandemonium: A demonstration of errors in complex beta-decay schemes. *Phys. Lett. B* **71**, 307–310 (1977) [https://doi.org/10.1016/0370-2693\(77\)90223-4](https://doi.org/10.1016/0370-2693(77)90223-4)

[9] Zakari-Issoufou, A.A., *et al.*: Total Absorption Spectroscopy Study of ${}^{92}\text{Rb}$ Decay: A Major Contributor to Reactor Antineutrino Spectrum Shape. *Phys. Rev. Lett.* **115**(10), 102503 (2015) <https://doi.org/10.1103/PhysRevLett.115.102503> arXiv:1504.05812 [nucl-ex]

[10] Haselschwardt, S.J., Kostensalo, J., Mougeot, X., Suhonen, J.: Improved calculations of beta decay backgrounds to new physics in liquid xenon detectors. *Phys. Rev. C* **102**, 065501 (2020) <https://doi.org/10.1103/PhysRevC.102.065501> arXiv:2007.13686 [hep-ex]

[11] Zhu, S., McCutchan, E.A.: Nuclear Data Sheets for $A=214$. *Nucl. Data Sheets* **175**, 1–149 (2021) <https://doi.org/10.1016/j.nds.2021.06.001>

[12] Wu, S.-C.: Nuclear Data Sheets for $A = 214$. *Nucl. Data Sheets* **110**, 681–748 (2009) <https://doi.org/10.1016/j.nds.2009.02.002>

[13] http://www.lnhb.fr/home/conferences-publications/ddep_wg/

[14] <https://www.nndc.bnl.gov/nudat3/>

[15] Lingeman, E.W.A., Konijn, J., Polak, P., Wapstra, A.H.: The decay of ${}^{214}\text{Pb}$ and other ${}^{226}\text{Ra}$ daughters. *Nuclear Physics A* **133**(3), 630–647 (1969) [https://doi.org/10.1016/0375-9474\(69\)90562-4](https://doi.org/10.1016/0375-9474(69)90562-4)

[16] Si, L., *et al.*: Determination of Double Beta Decay Half-Life of ${}^{136}\text{Xe}$ with the PandaX-4T Natural Xenon Detector. *Research* **2022**, 9798721 (2022) <https://doi.org/10.34133/2022/9798721> arXiv:2205.12809 [nucl-ex]

[17] Yan, X., *et al.*: Searching for Two-Neutrino and Neutrinoless Double Beta Decay of Xe^{134} with the PandaX-4T Experiment. *Phys. Rev. Lett.* **132**(15), 152502 (2024) <https://doi.org/10.1103/PhysRevLett.132.152502> arXiv:2312.15632 [nucl-ex]

[18] Li, T., *et al.*: Search for MeV-Scale Axionlike Particles and Dark Photons with PandaX-4T. *Phys. Rev. Lett.* **134**(7), 071004 (2025) <https://doi.org/10.1103/PhysRevLett.134.071004> arXiv:2409.00773 [hep-ex]

[19] Meng, Y., *et al.*: Dark Matter Search Results from the PandaX-4T Commissioning Run. *Phys. Rev. Lett.* **127**(26), 261802 (2021) <https://doi.org/10.1103/PhysRevLett.127.261802> arXiv:2107.13438 [hep-ex]

[20] Haaranen, M., Kotila, J., Suhonen, J.: Spectrum-shape method and the next-to-leading-order terms of the β -decay shape factor. *Physical Review C* **95**(2), 024327 (2017) <https://doi.org/10.1103/physrevc.95.024327>

[21] Hayen, L., Severijns, N., Bodek, K., Rozpedzik, D., Mougeot, X.: High precision analytical description of the allowed β spectrum shape. *Reviews of Modern Physics* **90** (2018)

[22] Nițescu, O., Stoica, S., Šimkovic, F.: Exchange correction for allowed β decay. *Physical Review C* **107**(2), 025501 (2023) <https://doi.org/10.1103/physrevc.107.025501>

[23] Suhonen, J.: *From Nucleons to Nucleus: Concepts of Microscopic Nuclear Theory*. Springer, Berlin (2007)

[24] Ramalho, M., Suhonen, J.: Computed total β -electron spectra for decays of Pb and Bi in the $^{220,222}\text{Rn}$ radioactive chains. *Physical Review C* **109**(1) (2024) <https://doi.org/10.1103/physrevc.109.014326>

[25] Ramalho, M., Suhonen, J.: g_A -sensitive β spectral shapes in the mass $A = 86\text{--}99$ region assessed by the nuclear shell model. *Physical Review C* **109**(3), 034321 (2024) <https://doi.org/10.1103/physrevc.109.034321>

[26] Ramalho, M., Suhonen, J., Neacsu, A., Stoica, S.: Spectral shapes of second-forbidden single-transition nonunique β decays assessed using the nuclear shell model. *Frontiers in Physics* **12**, 1455778 (2024) <https://doi.org/10.3389/fphy.2024.1455778>

[27] Warburton, E.K.: First-forbidden β decay in the lead region and mesonic enhancement of the weak axial current. *Physical Review C* **44**, 233–260 (1991)

[28] Shimizu, N., Mizusaki, T., Utsuno, Y., Tsunoda, Y.: Thick-restart block lanczos method for large-scale shell-model calculations. *Computer Physics Communications* **244**, 372–384 (2019) <https://doi.org/10.1016/j.cpc.2019.06.011>

[29] Warburton, E.K., Brown, B.A.: Appraisal of the Kuo-Herling shell-model interaction and application to $A = 210\text{--}212$ nuclei. *Physical Review C* **43**, 602–617 (1991)

[30] Brown, B.A., Rae, W.D.M.: The shell-model code NuShellX@MSU. *Nuclear Data Sheets* **120**, 115 (2014)

[31] Behrens, H., Buhring, W.: *Electron Radial Wave Functions and Nuclear Beta-decay* (International Series of Monographs on Physics). Clarendon Press, Oxford (1982)

[32] Kostensalo, J., Suhonen, J.: Mesonic enhancement of the weak axial charge and its effect on the half-lives and spectral shapes of first-forbidden $J^+ \leftrightarrow J^-$ decays. *Physics Letters B* **781**, 480–484 (2018) <https://doi.org/10.1016/j.physletb.2018.02.053>

[33] Chen, X., *et al.*: BambooMC — A Geant4-based simulation program for the PandaX experiments. *JINST* **16**(09), 09004 (2021) <https://doi.org/10.1088/1748-0221/16/09/T09004> arXiv:2107.05935 [physics.ins-det]